

Reflection and diffraction separation in the dip-angle common-image gathers using convolutional neural network

Jiaxing Sun¹, Jidong Yang¹, Zhenchun Li¹, Jianping Huang¹, Jie Xu¹, and Subin Zhuang¹

ABSTRACT

In exploration seismology, reflections have been extensively used for imaging and inversion to detect hydrocarbon and mine resources, which are generated from subsurface continuous impedance interfaces. When the interface is not continuous and its size reduces to less than half-wavelength, reflected wave becomes diffraction. Reflections and diffractions can be used to image subsurface targets, and the latter is helpful to resolve small-scale discontinuities, such as fault plane, pinch out, Karst caves, and salt edge. However, the amplitudes of diffractions are usually much weaker than that of reflections. This makes it difficult to directly identify and extract diffractions from unmigrated common-shot or common-middle-point gathers. Migrating seismic data into a subsurface location for different reflector dip angles yields a dip-angle-domain common-image gather (DACIG). One DACIG represents the migrated traces at a

fixed lateral position for different reflector dips. The reflection and diffraction have different geometric characteristics in DACIG, which provides one opportunity to separate diffractions and reflections. In this study, we present an efficient and accurate diffraction separation and imaging method using a convolutional neural network (CNN). The training data set of DACIGs is generated using one pass of seismic modeling and migration for velocity models with and without artificial scatterers, respectively. Then, a simplified end-to-end CNN is trained to identify and extract reflections from the migrated DACIGs that contain reflections and diffractions. Next, two adaptive subtraction strategies are presented to compute the diffraction DACIGs and stacked images, respectively. Numerical experiments for synthetic and field data demonstrate that the proposed method can produce accurate reflection and diffraction separation results in DACIGs, and the stacked image has a good resolution for subsurface small-scale discontinuities.

INTRODUCTION

In exploration seismology, the reflections have been extensively used in imaging and inversion to map subsurface continuous impedance interfaces (Riley and Claerbout, 1976; Yilmaz and Claerbout, 1980; Ronen and Claerbout, 1985). Seismic diffractions are generated from local discontinuous objects that are less than half-wavelength (Krey, 1952; Kunz, 1960; Aki, 1969; Sato, 1977; Landa et al., 1987; Kanasewich and Phadke, 1988). This specific characteristic of diffractions provides an opportunity to resolve subsurface small-scale structures, such as fault plane, pinch out, Karst caves, and salt boundary. However, in the data domain, the amplitudes of diffractions are usually one order of magnitude weaker than those of the reflections, resulting in that they are submerged in strong reflec-

tions (Klokov et al., 2010b; Zhao et al., 2016). In addition, the reflections and diffractions appear to be hyperbolas in common-shot gathers. The large amplitude difference and similar geometric characteristics make them difficult to be separated from unmigrated common-shot or common-middle-point data.

Diffraction imaging is an important tool for identifying the subsurface discontinuities, which are sometimes the prospecting targets in exploration seismology. In early studies, many approaches have been developed to separate the diffractions and reflections. For example, Harlan et al. (1984) isolate the weak diffraction signals based on a statistical tool in the local slant-stack domain. Subsequently, the diffraction separation is applied to the poststack sections for ground penetration radar data (Papziner and Nick, 1998) and seismic data (Dell and Gajewski, 2011). Using the plane-wave destruc-

Manuscript received by the Editor 17 March 2022; revised manuscript received 3 September 2022; published ahead of production 24 October 2022; published online 28 December 2022.

¹School of Geosciences, Laboratory for Marine Mineral Resources, and National Laboratory for Marine Science and Technology, Key Laboratory of Deep Oil and Gas, China University of Petroleum(East China), Qingdao, Shandong, China. E-mail: sjx2891969901@163.com; jidong.yang@upc.edu.cn (corresponding author); jphuang@upc.edu.cn (corresponding author); 19830010@upc.edu.cn; 1701040128@s.upc.edu.cn; subin_zhuang@163.com.

© 2023 Society of Exploration Geophysicists. All rights reserved.

tion filter, Fomel et al. (2007) extract and image the diffraction events in zero-offset data volume, which helps to enhance the imaging accuracy of small-scale discontinuities. Bauer et al. (2021) apply the neural network to extract diffractions on the stacked image according to reflection and diffraction curvatures and also show a great potential for ground-penetrating radar data. In addition, the diffractions can be extracted from the prestack gathers. For instance, the focusing-muting-focusing strategy on common-shot gathers is used to improve diffractor image resolution (Khaidukov et al., 2004). The plane-wave destruction filter is used by Taner et al. (2006) to suppress specular reflection events and extract diffractions. Bauer et al. (2016) propose a diffraction traveltime decomposition principle based on the decoupling of up- and downgoing raypaths to produce accurate diffraction wavefield attributes. The wavefront attributes have been used to separate diffractions and improve diffraction velocity spectra quality (Bakhtiari Rad et al., 2018). Schwarz (2019) proposes a data-driven diffraction separation method using the coherent wavefield subtraction and recovers the diffraction with accurate amplitudes and phases for prestack and poststack 2D and 3D data.

In the migration, mapping seismic data into a subsurface location for different reflector dip angles yields a dip-angle-domain common-image gather (DACIG). The diffraction and reflection have different geometric characteristics in DACIGs (Audebert et al., 2002; Landa et al., 2008; Reshef and Landa, 2009). If the migration velocity is accurate, the diffraction appears as a flat event, whereas the reflection is concaved (“smile”) with a stationary phase apex. Based on this observation, many diffraction separation methods have been developed in the dip-angle domain. Landa et al. (2008) use a plane-wave destruction filter to suppress the reflections in DACIGs. Klokov et al. (2010a) introduce a diffraction and reflection separation method by removing the reflection apex in the hybrid Radon domain. Subsequently, Klokov and Fomel (2012) apply hybrid Radon transform to produce diffraction and reflection-only DACIGs. Zhang and Zhang (2014) attenuate reflections by muting the Fresnel zones in the shot and opening-angle gathers generated by prestack time migration. Dafni and Symes (2017) implement the diffraction separation in the DACIGs by applying a dip-domain specularity filter. Tschannen et al. (2020) use the deep learning method to automatically map and identify the locations of diffractor from the DACIGs. Li et al. (2020) use a Mahalanobis and phase-based attenuation function to suppress reflections and extract diffractions in full-azimuth CIGs. Once the diffractions are extracted in the angle domain, the diffractor image can be obtained by summing them over the dip angles, which is helpful to resolve small-scale geologic targets.

Deep learning is a data-driven statistical method and has been widely applied for many geoscience problems. In particular, convolutional neural network (CNN) uses multiple hidden layers and can efficiently recognize specific data and image patterns. For example, the CNN has been used to attenuate random noise while not degrading effective signals to improve seismic data signal-to-noise ratio (Wang and Chen, 2019; Yu et al., 2019). Recently, a few works apply the CNN to learn the patterns of subsurface salt bodies and implement automatic salt-body classification to detect subsalt reservoirs (Waldegaard and Solberg, 2017; Di et al., 2018; Karchevskiy et al., 2018; Shi et al., 2018). Based on different features among the first break and later events, the CNN has been applied to quickly pick the first arrival from common-shot seismic data (Hollander et al., 2018; Yuan et al., 2018). There are some attempts to apply the CNN to recover subsurface velocity models from surface ob-

served seismic data, which show that the CNN has potential to solve the inversion problem (Biswas et al., 2019; Das et al., 2019; Zheng et al., 2019; Wang et al., 2022). In addition, the CNN has been introduced in the full-waveform inversion to estimate velocity model to mitigate the ill-posedness and cycle-skipping issues (Jin et al., 2018; Wu and McMechan, 2018; Wu and Lin, 2019). Many CNN-based methods, such as LeNet, U-net, and VGG-Net, have been developed to automatically identify and map the faults in seismic interpretation (Pochet et al., 2018; Wu et al., 2018, 2019a, 2019b; Xiong et al., 2018). However, CNN has some limitations. For instance, it needs a large number of training data sets to build a reliable network, and the application of trained neural network to unseen data may produce a completely incorrect result. To mitigate this problem, Wang et al. (2019) introduce a stationary random matrix to increase the training data and effectively reduce the biased fitting issue. Wu et al. (2020) propose to build diverse geologic models with typical folds and faults to increase data diversity.

In this study, we present an efficient and accurate CNN-based diffraction separation and imaging method in the migrated dip-angle domain. The training data of DACIGs are generated using one pass of seismic modeling and migration for velocity models with and without artificial scatterers. Then, a simplified end-to-end CNN architecture is trained to identify and extract reflection response from the DACIGs those contain reflections and diffractions. Next, two adaptive subtraction strategies are proposed to compute the diffraction-only DACIGs and stacked images. One is to directly compute the diffraction gathers by adaptively subtracting the CNN predicted reflections from the total input gathers, followed by a stacking to yield the diffractor image. The other is to first calculate a reflector image by stacking the predicted reflection-only DACIGs and then to compute the diffractor image by adaptively subtracting the reflector image from the total stacked image. Numerical examples demonstrate that the proposed method can produce accurate reflection and diffraction gathers and stacked images.

The rest of this paper is organized as follows. We first give a brief overview about the characteristics of reflection and diffraction in the dip-angle domain. Then, the proposed reflection and diffraction separation method is described in detail. Finally, the numerical experiments of two synthetic and one field data are used to test the performance of the proposed method.

METHODOLOGY

The characteristics of diffraction and reflection in the dip-angle domain

As analyzed by Landa et al. (2008), in a homogeneous medium, the reflection event in the dip-angle domain can be expressed as

$$z_\alpha(x, \alpha) = \frac{(z_0 \cos \alpha_0 + x \sin \alpha_0)v_M \cos \alpha}{v - v_M \sin \alpha_0 \sin \alpha}, \quad (1)$$

whereas the diffraction event has the form

$$z_\alpha(x, \alpha) = \frac{v_M \cos \alpha [(x - x_0)v_M \sin \alpha + D]}{v^2 - v_M^2 \sin^2 \alpha}, \quad (2)$$

where $D = \sqrt{z_0^2(v^2 - v_M^2 \sin^2 \alpha) + (x - x_0)^2 v^2}$, v is the true velocity model, v_M is the migration velocity model, α_0 is the dip angle of a reflector, α is the migration angle, (x, z_α) denotes the DACIG index,

and (x_0, z_0) denotes a diffraction point location. The theoretical responses of a diffractor and reflector in the dip-angle domain are shown in Figure 1. When the migration velocity is accurate, the diffraction response is flat, whereas the reflection appears as a smile with a stationary point. When the migration velocity is inaccurate, the reflection event still keeps an up-curved shape, but the diffraction is no longer a linear event. In addition, if the diffractor is away from the DACIG location, the diffraction becomes a dipping event without a stationary point.

Two typical DACIGs are shown in Figure 2 to illustrate the different characteristics of diffraction and reflection responses. The DACIGs are computed using Gaussian beam depth migration (Hill, 1990; Yang et al., 2021) with accurate and inaccurate migration velocity models. When the migration velocity is accurate (Figure 2a), the reflection events highlighted by the yellow arrows show concaved shapes, whereas the diffraction indicated by the red arrow is flattened. In contrast, the nearby diffractors generate dipping linear events in the gathers (the blue arrows in Figure 2a). The degree of dipping is determined by lateral distance between the diffractor and DACIG locations. When the migration velocity is inaccurate, the diffraction event becomes curved and has no stationary point (the red arrow in Figure 2b). The reflections still keep the smile shapes, but their locations move downward (the yellow arrows in Figure 2b). This example demonstrates that the diffractions and reflections have different geometric characteristics in the migrated dip-angle domain. This indicates that the reflections and diffractions can be separated in the DACIGs by identifying different linear and concaved features.

CNN architecture

In this section, we use a simplified denoising CNN (DnCNN) (Zhang et al., 2017) to separate the diffractions and reflections in DACIGs. The modified end-to-end CNN has three partitions. The first partition consists of a convolutional layer and a rectified linear unit (ReLU), in which the ReLU is used to improve the non-linear mapping ability of the network. In the second partition, the convolution, batch normalization (BN), and ReLU activation function are repeatedly applied, of which the BN operator is used to speed up training (Ioffe and Szegedy, 2015). A convolutional layer is used in the last part of the network. The inputs for the simplified

end-to-end CNN architecture are the DACIGs that have reflections and diffractions, and the outputs are the reflection DACIGs. Unlike the original DnCNN that tries to predict noise from observed data, our network is trained to extract the curved reflection events from the total DACIGs. The kernel size is set as 7×7 , and the number of feature map channels is 64. The hidden layer number is set as 10. With sufficient epochs for training, the proposed network can accurately predict the reflection-only DACIGs, and the diffraction DACIGs and stacked images can be computed by applying an adaptive subtraction (the details are presented subsequently).

Hyperparameter tuning

The network training is carried out on two Quadro RTX 5000 NVIDIA graphical processing units using the Adam optimizer (Kingma and Ba, 2014). The accuracy of network prediction results is highly dependent on the hyperparameter settings (Mantovani et al., 2015). Thus, we test many hyperparameters in the training

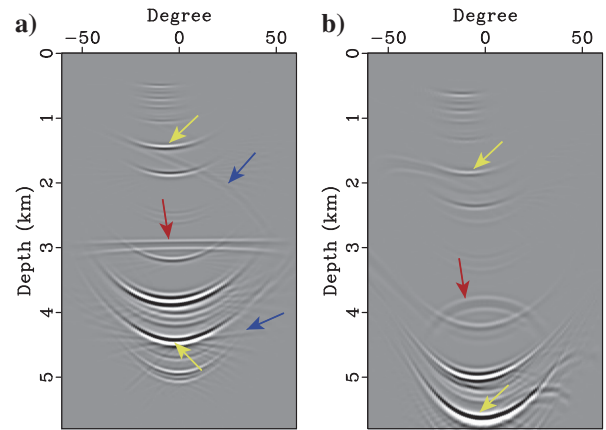


Figure 2. The DACIGs are generated using seismic modeling and migration for (a) the accurate velocity model and (b) a lower velocity model. The yellow and red arrows denote the reflection and diffraction responses generated by the reflector and diffractor of the gather location, respectively. The blue arrows indicate the diffraction responses generated by the diffractors far away from this gather location.

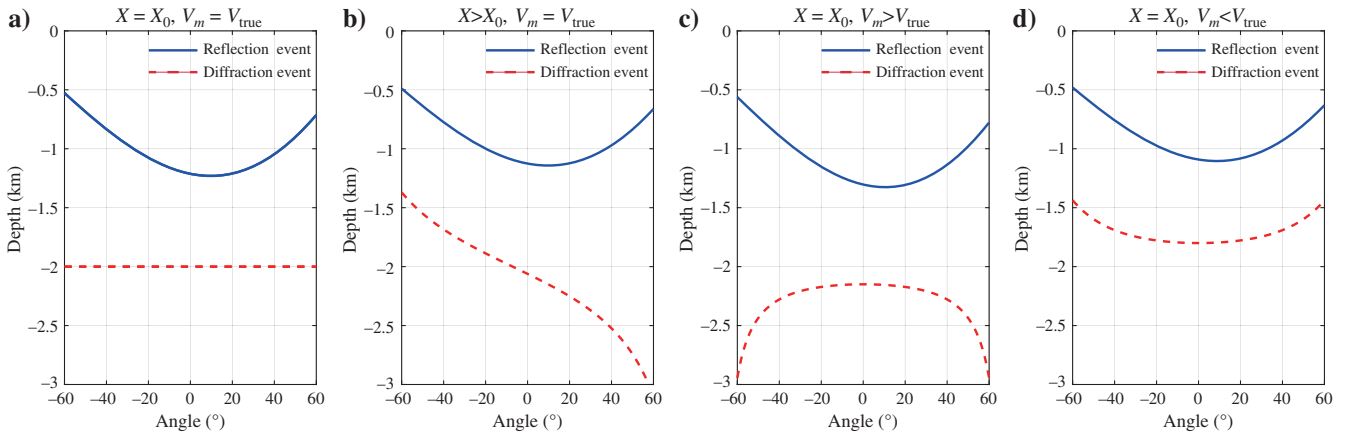


Figure 1. Theoretical DACIGs for a scatterer and a reflector with different velocity models and DACIG locations. The dashed red curves represent the diffraction events and the solid blue curves denote the reflection responses. (a and b) The results with accurate velocity but with DACIG consistent and away from scatterer location, respectively. (c and d) The results with higher and lower velocity models, respectively.

process using the training and validation data sets and finally find an optimal CNN architecture. The optimized network setting is as follows:

- 1) The sliding stride of the convolutional kernel over the input gathers is fixed to one depth sample after many tests for different strides.
- 2) Zero padding is used to ensure the network input and output images having the same size.
- 3) The mean-squared error is used as the loss function to measure the misfit between the prediction results and labeled data.
- 4) The network initial weights are generated using the “He” initialization (He et al., 2015), which can mitigate the rectifier nonlinearities and avoid gradient vanishing of deep layers during the forward and backward propagation.
- 5) The learning rate for updating the network weights is set as 0.001.

- 6) The maximum epoch of network training is 50 and increasing the epoch does not significantly improve the prediction accuracy.
- 7) The mini-batch size for the input DACIGs is 128.

Adaptive subtraction

In seismic processing, the adaptive subtraction is commonly used in the multiples removal for marine streamer data. Because the predicted multiples may have different amplitude, frequency, and phase from the multiples in the observed data, directly subtracting the predicted multiples from the observed data cannot remove the multiples accurately and lead to strong residual energy. Therefore, a matching filter should be used to correct the amplitude and frequency spectrum of the predicted multiples to match the real multiples (Herrmann et al., 2008). Here, we apply the adaptive subtraction to remove the reflections from total DACIGs or the stacked image. The CNN predicted reflection $\mathbf{I}_{\text{ref}}^{\text{pre}}$ can be matched to that in the total dip-angle gather or on the stacked image $\mathbf{I}_{\text{ref}}^{\text{obs}}$ as

$$\mathbf{I}_{\text{ref}}^{\text{obs}} \approx \mathbf{C}^{-1} \text{diag}\{\mathbf{w}\} \mathbf{C} \mathbf{I}_{\text{ref}}^{\text{pre}}, \quad (3)$$

where \mathbf{w} is a scaling vector that relates the $\mathbf{I}_{\text{ref}}^{\text{pre}}$ to $\mathbf{I}_{\text{ref}}^{\text{obs}}$ in the curvelet domain and \mathbf{C} is a discrete curvelet transform.

To avoid undeterminedness caused by curvelet transform and overfitting issue, the equation 3 can be modified by adding a regularization term as

$$\begin{bmatrix} \mathbf{I}_{\text{total}}^{\text{obs}} \\ 0 \end{bmatrix} = \begin{bmatrix} \mathbf{C}^{-1} \text{diag}\{\mathbf{C} \mathbf{I}_{\text{ref}}^{\text{pre}}\} \\ \gamma \mathbf{L} \end{bmatrix} \mathbf{w}, \quad (4)$$

where $\mathbf{I}_{\text{total}}^{\text{obs}}$ is the total DACIG or stacked image and can be expressed as $\mathbf{I}_{\text{total}}^{\text{obs}} = \mathbf{I}_{\text{rel}}^{\text{obs}} + \mathbf{I}_{\text{dif}}^{\text{obs}}$, $\mathbf{I}_{\text{dif}}^{\text{obs}}$ is the diffraction DACIG or stacked diffractor image, \mathbf{L} is a sharpening operator to promote smooth constraint on the solution \mathbf{w} , and γ controls the degree of smoothness.

The scaling vector \mathbf{w} can be solved by minimizing the following misfit function:

$$J(\mathbf{w}) = \frac{1}{2} \|\mathbf{I} - \mathbf{F}\mathbf{w}\|_2^2. \quad (5)$$

The preceding problem can be solved using a Broyden-Fletcher-Goldfarb-Shanno algorithm (He et al., 2015), and the gradient is

$$\text{grad}J(\mathbf{w}) = \text{diag}\{\mathbf{w}\} [\mathbf{F}^T (\mathbf{F}\mathbf{w} - \mathbf{I})], \quad (6)$$

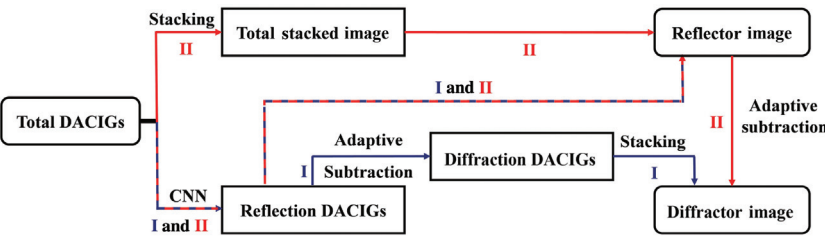


Figure 3. Two strategies to compute diffraction DACIGs and stacked images. The blue arrows represent the strategy I, and the red arrows represent the strategy II.

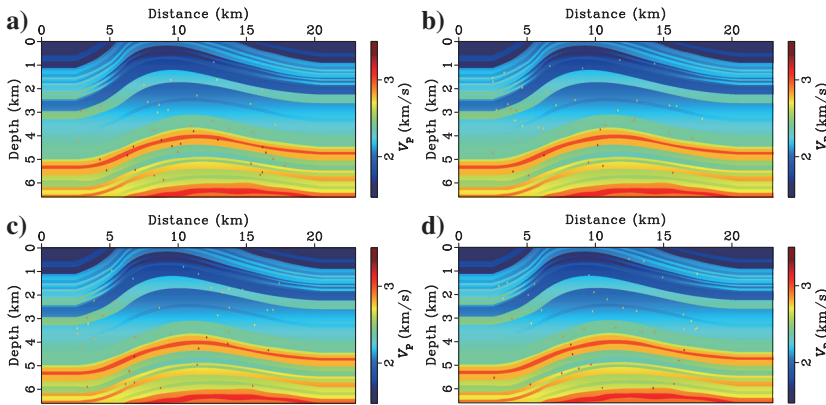


Figure 4. Four velocity models constructed by randomly adding artificial scatterers to the right portion of Marmousi-II model.

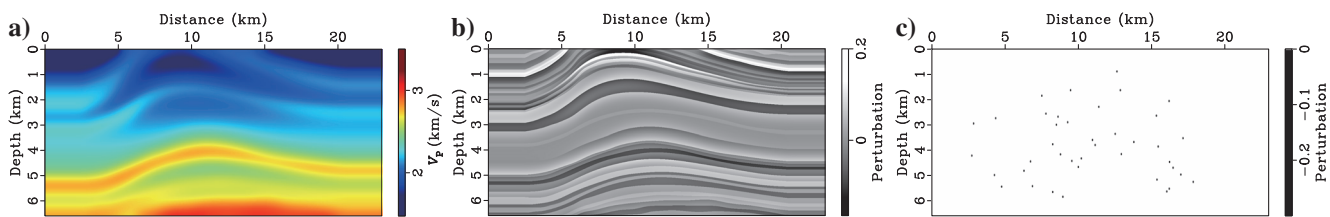


Figure 5. Models used for computing DACIGs. (a) The smoothed P-wave velocity model. (b and c) The reflectivity models of reflectors and diffractors, respectively.

where

$$\mathbf{F} = \begin{bmatrix} \mathbf{C}^{-1} \text{diag}\{\mathbf{CI}_{\text{ref}}^{\text{pre}}\} \\ \gamma \mathbf{L} \end{bmatrix} \quad \text{and} \quad \mathbf{I} = \begin{bmatrix} \mathbf{I}_{\text{total}} \\ \mathbf{0} \end{bmatrix}. \quad (7)$$

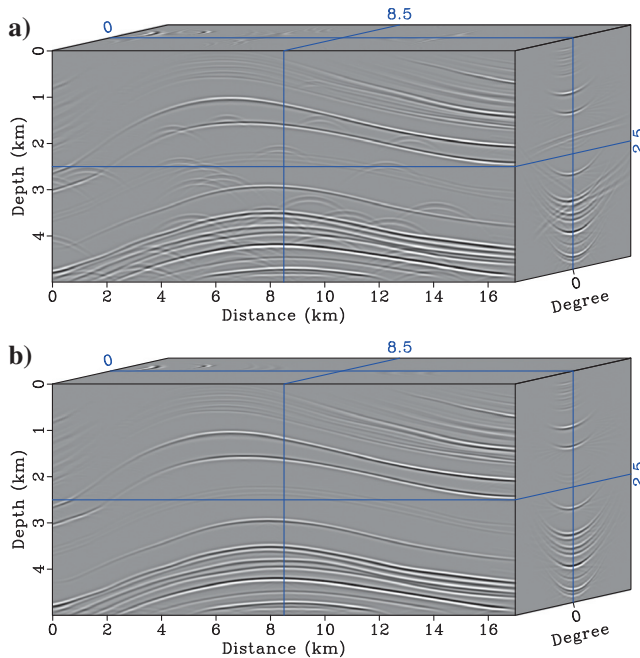


Figure 6. A representative training data set computed using one of velocity model shown in Figure 4. (a) The total DACIGs computed using a velocity model with artificial scatterers. (b) The reflection-only DACIGs computed using a velocity model without scatterers.

Diffraction separation and imaging workflow

The workflow of the proposed diffraction separation and imaging using the CNN can be summarized as the following steps:

- 1) Using realistic velocity models with and without artificial point scatterers to simulate seismic records by solving the wave equation using a finite-difference method.
- 2) Migrating synthetic records to generate the DACIGs and stacked image using any available seismic migration approaches.
- 3) Using the DACIGs that contain reflections and diffractions as the network input and using the DACIGs that only have reflections as the labeled data.
- 4) Using the input DACIGs and labeled data to train the proposed CNN architecture.
- 5) Applying the trained CNN to the test data set of DACIGs to predict the reflection patterns.
- 6) Calculating the diffraction DACIGs and stacked images using an adaptive subtraction.

In the sixth step, we use two strategies to implement the adaptive subtraction (Figure 3). One is to adaptively subtract the predicted reflection DACIGs from the input gathers, and then stack the resulting diffraction DACIGs to produce a diffractor image. The other strategy is first to compute the reflector image by stacking the predicted reflection DACIGs, and then the diffractor image is calculated by adaptively subtracting the reflector image from the total stacked image.

NUMERICAL EXPERIMENTS

In this section, we use Marmousi-II model, Sigsbee 2A model, and one field data to demonstrate the performance and adaptability of the proposed CNN-based reflection and diffraction separation method.

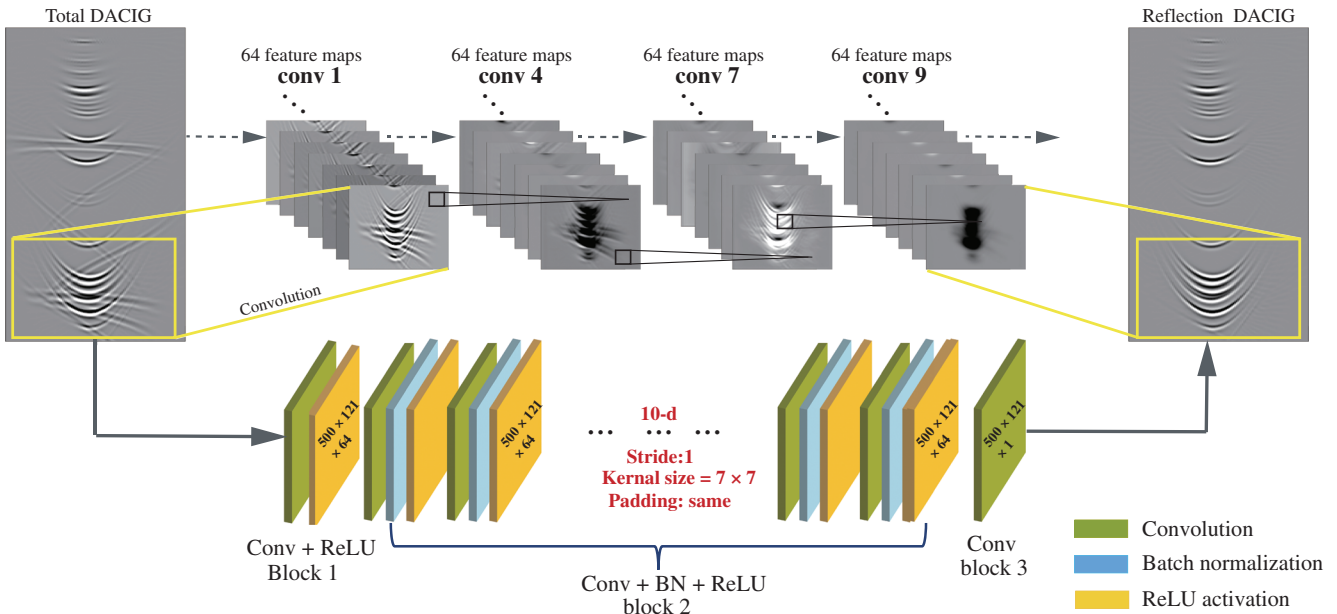


Figure 7. The simplified end-to-end CNN architecture used for diffraction separation. The total DACIG image is used as the input of network, and the network generates 64 feature maps for each convolutional layer. The output image is the reflection DACIGs. The network contains three blocks: Conv + ReLU, Conv + BN + ReLU, and Conv. Different colors represent different operators.

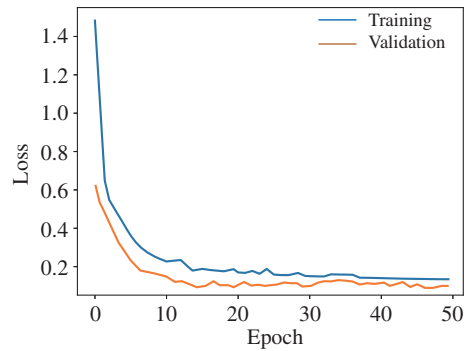


Figure 8. The loss curves of the CNN model.

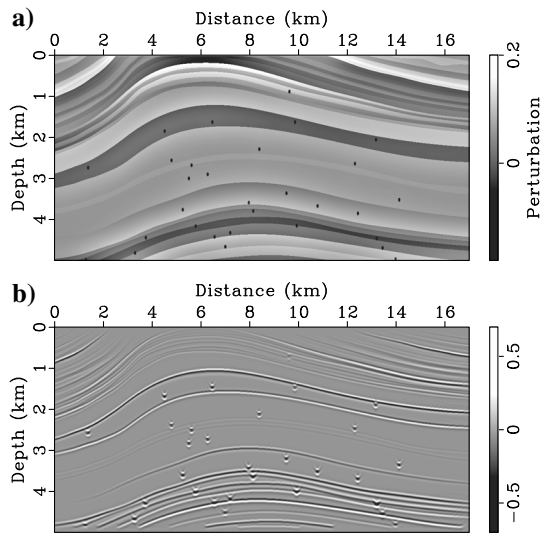


Figure 9. The experiment of diffraction separation for the Mar-mousi-II model. (a) The true reflectivity model. (b) Total image computed using the Gaussian beam depth migration.

Figure 10. The feature maps extracted from the original seismic image at different convolutional layers. Each row shows the feature maps generated in the same convolutional layer. Each column shows the feature maps generated in the different convolutional layers.

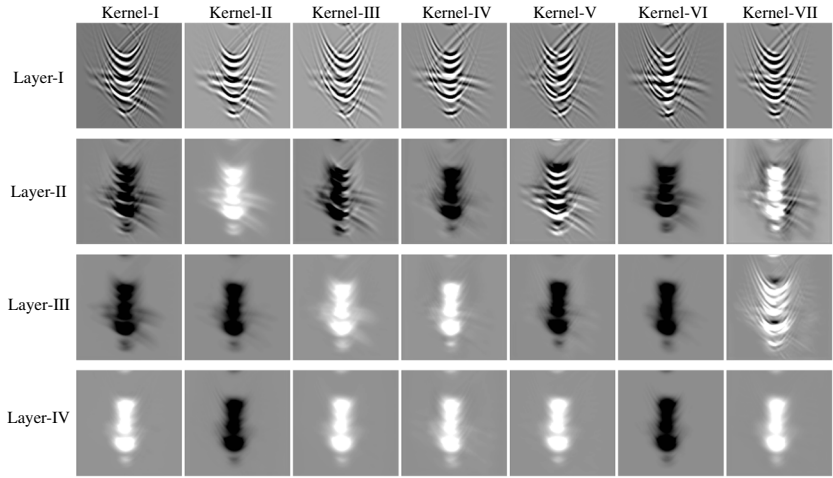
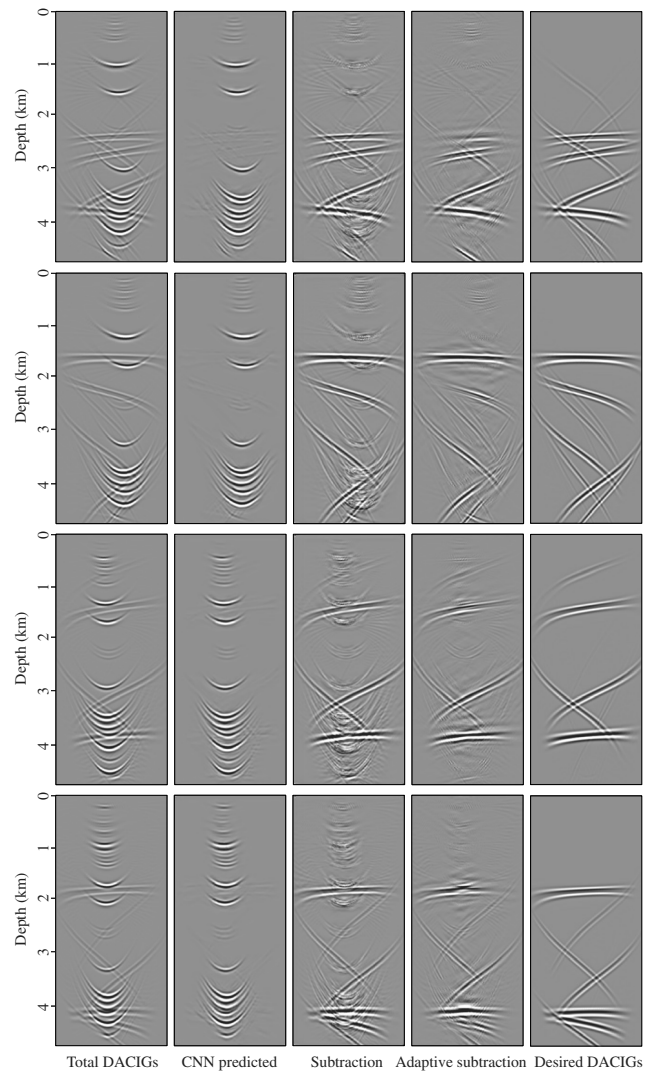


Figure 11. The DACIGs at four different positions. Each row corresponds to one location. The first column is the total DACIG. The second column is the predicted reflection DACIG by CNN method. The third and fourth columns are the direct and adaptive subtraction results, respectively. The fifth column is the desired DACIGs.



Training data sets

We use a portion of the Marmousi-II model to build the training data set, which only contains continuous reflectors. To generate diffractions in seismic records, we randomly add artificial point scatterers in the original velocity model. Four new velocity models are built as shown in Figure 4. Two DACIG sets are generated using seismic modeling and migration: one for the model only with reflectors and the other with reflectors and artificial scatterers. The model is discretized onto a 2300×650 grid with a 10 m spacing. A smoothed velocity model (Figure 5a) is used in the migration, and the true reflectivity models for reflectors and scatterers are shown in Figure 5b and 5c. The Ricker wavelet with a peak frequency of 10 Hz is used as the source time function. A total of 180 shots are evenly distributed on the surface with a source increment of 100 m. Each shot is recorded by 500 receivers with a spacing of 10 m. The time interval in the modeling is 1 ms, and the record duration is 6 s. Figure 6 shows one set of representative total and reflection-only DACIGs. The total DACIGs contain flattened diffractions and concaved reflections, in which the reflection energy is larger than the diffraction. The reflection DACIGs only contain concaved events. We generate 1700 pairs of reflection-only and total DACIGs to train the proposed CNN architecture (Figure 7), in which 1500 pairs are randomly selected as the training set, and the other 200 pairs are used as the validation set to estimate loss during the training. The loss curves of training and validation shown in Figure 8 are reduced significantly in the first 30 epochs and tend to be stable after 30 epochs. This indicates that the designed CNN framework has converged to an accurate solution after a dozen of iterations.

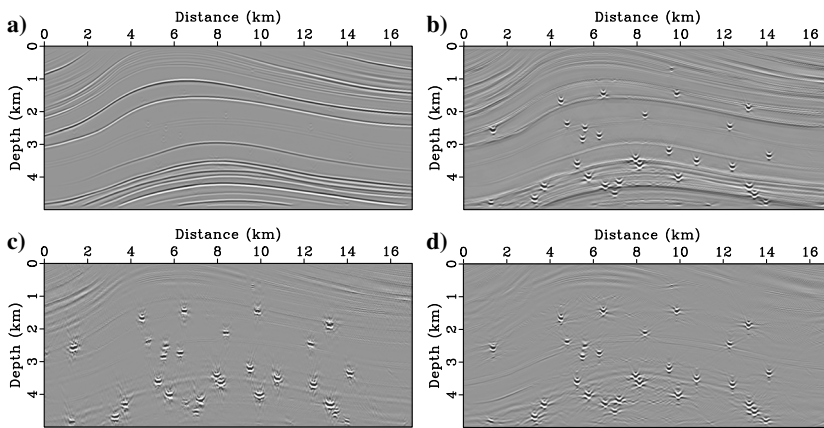


Figure 12. (a) Reflector and (b-d) diffractor images. (a) Computed by stacking the CNN predicted DACIGs. (b) Calculated by stacking the residual diffraction DACIGs computed using direct subtraction. (c) The diffractor image computed using the adaptively subtracted DACIGs. (d) Computed by adaptively subtracting the stacked reflector image (a) from total image (Figure 9b).

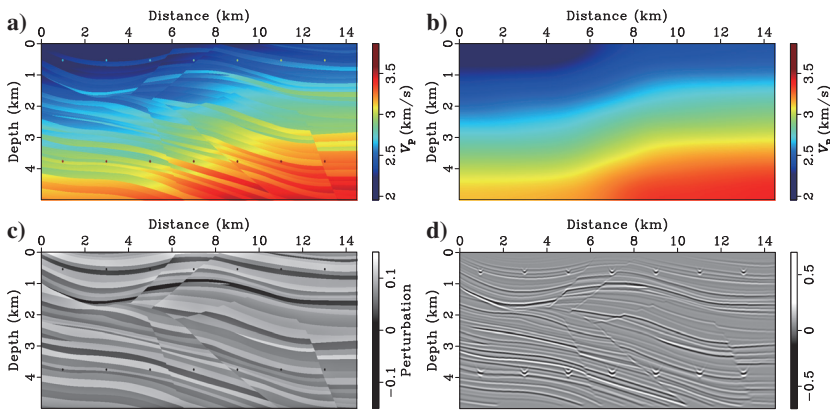


Figure 13. The experiment of diffraction separation for the Sigsbee 2A model. (a-c) True velocity, smoothed velocity, and true reflectivity models, respectively. (d) Total image computed using the Gaussian beam depth migration.

The validation for Marmousi-II model

In this section, we compute a total of 2300 pairs DACIGs independent of training and validation sets to test the performance of the proposed method. The total DACIGs and stacked images are computed using seismic modeling and Gaussian beam migration for the Marmousi-II model with artificial point scatterers (Figure 4a). The true reflectivity model is shown in Figure 9a. The migrated image using the data containing reflections and diffractions is shown in Figure 9b. Figure 10 shows the feature maps of the different hidden layers, which indicates that the proposed end-to-end CNN can effectively capture the reflection patterns of concaved events during the training process. The total DACIGs at four different locations are shown in the first column of Figure 11, and the predicted reflection DACIGs are shown in the second column. The corresponding stacked reflector image is shown in Figure 12a. The predicted reflection DACIGs only contain reflection events, which demonstrates that the reflection concave patterns have been accurately extracted by the trained network.

We first directly subtract the predicted reflection DACIGs from the total DACIGs. The residual diffraction DACIGs and the stacked diffractor image are shown in the third column of Figures 11 and 12b, respectively. Because of different amplitudes between the predicted and true reflections, the residual diffraction DACIGs and stacked image still contain strong reflections leakage. To mitigate this issue, we apply an adaptive subtraction for DACIGs and stacked images. The fourth and fifth columns of Figure 11 show the adaptive subtraction results and reference DACIGs, respectively. The reflection events are

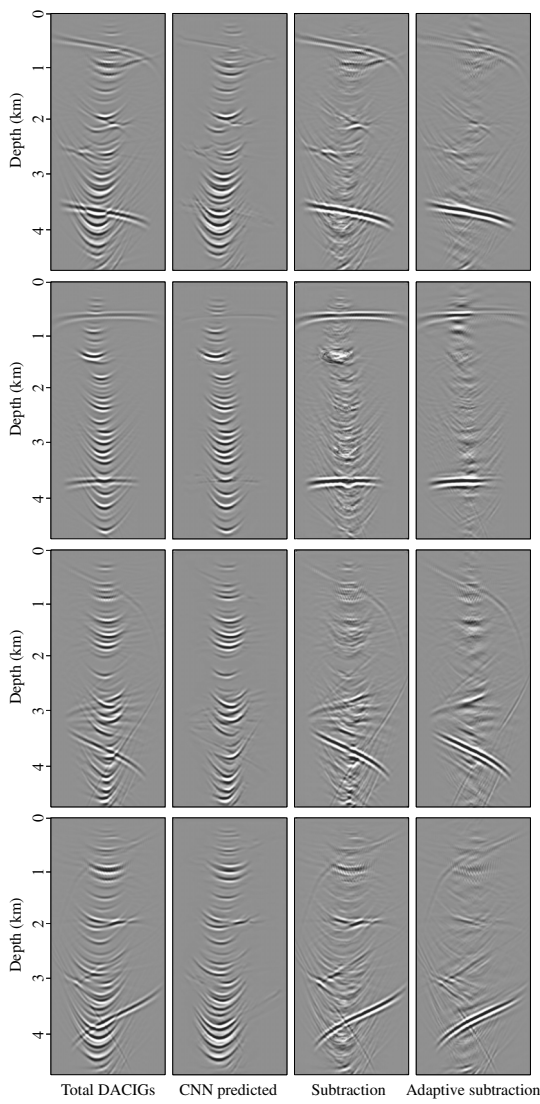
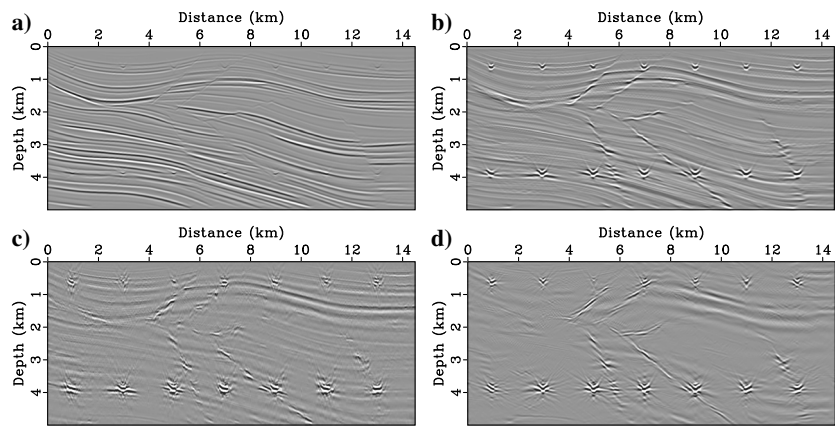


Figure 14. The DACIGs at four different positions. Each row corresponds to one location. The first column is the total DACIG. The second column is the predicted reflection DACIG by CNN method. The third and fourth columns are the direct and adaptive subtraction results, respectively.

Figure 15. (a) Reflector and (b–d) diffractor images. (a) Computed by stacking the CNN predicted DACIGs. (b) Calculated by stacking the residual diffraction DACIGs computed using direct subtraction. (c) The diffractor image computed using the adaptively subtracted DACIGs. (d) Computed by adaptively subtracting the stacked reflector image (a) from total image (Figure 13d).



mostly removed, and the weak diffractions are clearly extracted. Compared with the results in the third column of Figure 11, the adaptive subtraction results show that it can automatically remove the reflection patterns, no matter how different the amplitudes are between the predicted and true reflections and well match with the reference DACIGs. The stacked image is shown in Figure 12c, in which the point scatterers can be clearly identified. But the point scatterers are not focused well because the nearby diffraction DACIGs have weaker reflection energy. On the other hand, we use the adaptive subtraction for the stacked images rather than directly applying it on DACIGs. The stacked reflector image is adaptively subtracted from the total stacked image, and the corresponding diffractor image is shown in Figure 12d. The point scatterers are well imaged, and the continuous reflectors are attenuated. The resulting image is helpful to identify the small-scale diffractors, which are commonly important targets in the oil and gas exploration.

The application for Sigsbee 2A model

In this experiment, we use Sigsbee 2A model (Figure 13a) to test the transfer learning ability of the trained network for diffraction separation. The faults and point scatterers in the model can produce rich diffractions. The migration velocity and reflectivity models are shown in Figure 13b and 13c, respectively. We discretize this model with a grid of 1700×500 and a spatial spacing of 10 m. The Ricker wavelet with a peak frequency of 10 Hz is used as the source time function. A total of 95 shots are evenly distributed on the surface with an interval of 100 m, and 500 receivers are used to record data for each shot with a spacing of 10 m. Time sampling is 1 ms, and the record duration is 6 s. The stacked migration result for this model is shown in Figure 13d. In the diffraction separation test, we use the network trained with the data of Marmousi-II model and apply it to the DACIGs of Sigsbee 2A model.

The total and predicted reflection DACIGs at four different locations are shown in the first and second columns of Figure 14, respectively. The reflections from subsurface continuous reflectors are well recognized by the previously trained CNN. By stacking the predicted reflection DACIGs over dip angles, we obtain the reflector image (Figure 15a), on which the impedance interfaces are clearly resolved. The residual diffraction DACIGs calculated by direct subtraction are shown in the third column of Figure 14. The resulting diffraction DACIGs still contain undesired residual reflections and hence cannot be used to accurately detect small-scale scat-

terers (Figure 15b). In contrast, the adaptive subtraction can remove almost reflection events and produce clear diffraction DACIGs (the fourth column in Figure 14) and a high-resolution diffractor image (Figure 15c). In addition, we compute the diffractor image (Figure 15d) by adaptively subtracting the stacked reflector image from the total image, which has a higher signal-to-noise ratio than that in Figure 15c.

Application to field data

We use a field data set to test the adaptability of the proposed CNN-based diffraction separation method. Similar to the synthetic data examples, we use observed common-shot records (Figure 16a) and migration velocity model (Figure 16b) to calculate total DACIGs (the first column of each panel in Figure 17) and stacked image (Figure 18a) with the Gaussian beam migration. The velocity model is computed using a ray-based tomography method. The strong reflectors in Figure 18a can be clearly seen, and the high-amplitude reflection components in total DACIGs severely cover weak diffractions, which are related to subsurface discontinuities. To resolve small-scale structures, we first apply the CNN trained with Marmousi-II data sets to extract reflection events from total DACIGs. The separated reflection events (the second column of each panel in Figure 17) have larger apertures, and the reflection features are well preserved. Then, we adopt the second adaptive subtraction strategy to calculate a high-resolution diffractor image (Figure 18c) by adaptively subtracting the reflector image (Figure 18b) from the total stacked image. The proposed method for diffraction separation can provide valuable information about small-scale structure features, in which the faults marked with the yellow arrows can be accurately identified at a depth interval of 3–8 km and other discontinuities (the blue arrows) are clearly visible. The calculated diffractor image successfully reveals small-scale anomalies hidden in conventional image.

DISCUSSION

The transfer learning ability of the proposed CNN-based diffraction separation method largely depends on the diversity of the reflection and diffraction features. We select a right portion of the Marmousi-II model that only contains continuous reflectors to generate reflection-only DACIGs. In addition, we add artificial scatterers to the model to generate the DACIGs with reflections and diffractions. Using these two velocity models, we calculate a large number of realistic data sets for training the network. Numerical examples for two benchmark models and one field data demonstrate that the network trained by synthetic training data sets can accurately recognize

the reflection patterns. In particular, although the CNN is only trained on DACIGs of Marmousi-II models, we can obtain a high-resolution scatterer and fault image of Sigsbee 2A model and field data. This indicates a good transfer learning ability of the trained CNN. In this study, the synthetic diffractions only come from the point scatterers. To enhance the feature expression ability of the network, we will consider point and nonpoint scatterers to generate more realistic training data sets in the future.

The network architecture used in this study is a simplified DnCNN. The DnCNN is a well-known network architecture for image denoising (Zhang et al., 2017). The applications of the DnCNN for denoising and dediffractions share the same principle that attenuates one component while preserving other components. The DnCNN architecture is more complicated and time consuming for diffraction separation. Therefore, we simplify the previously published DnCNN by reducing the number of hidden layers. The experimental results demonstrate that the simplified end-to-end CNN can speed up the training process while producing satisfactory results. In our early tests, we use the total DACIGs as the input and the diffraction gathers as the labels to train the CNN. The resulting prediction for the diffraction gathers contains strong residual reflection energy, which further leads to inaccurate reflection and diffraction separation results. This might be caused by (1) relatively weak amplitudes of diffraction compared with reflections and (2) fewer diffractors in subsurface than reflectors. Then, we change to predict reflections in the dip-angle gathers and thus use the reflections as the labels.

The adaptive subtraction is used to match the true reflections with the CNN predicted reflections. We apply the adaptive subtraction strategy on the DACIGs and stacked image, respectively. The stacked image of a point scatterer is constructed by stacking a group

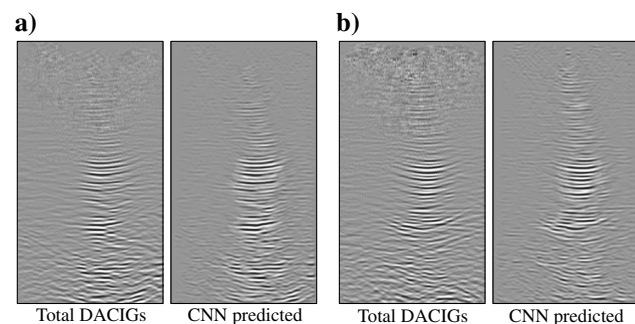


Figure 17. (a and b) The DACIGs at two different positions. The first column of each panel is the total DACIG. The second column of each panel is the predicted reflection DACIG by CNN method.

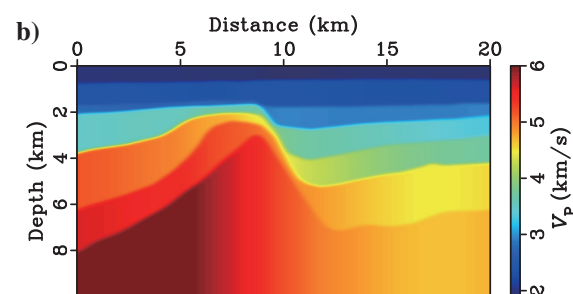
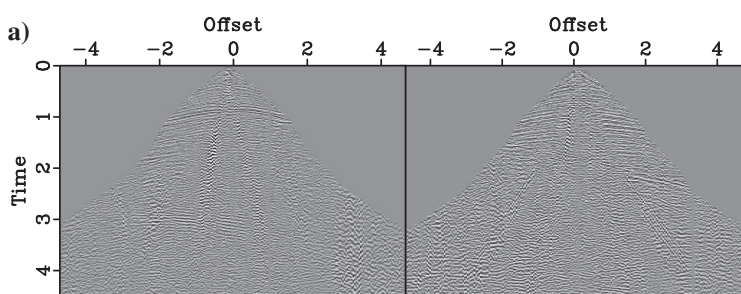


Figure 16. The field data for a land survey. (a and b) Common-source data and migration velocity model, respectively.

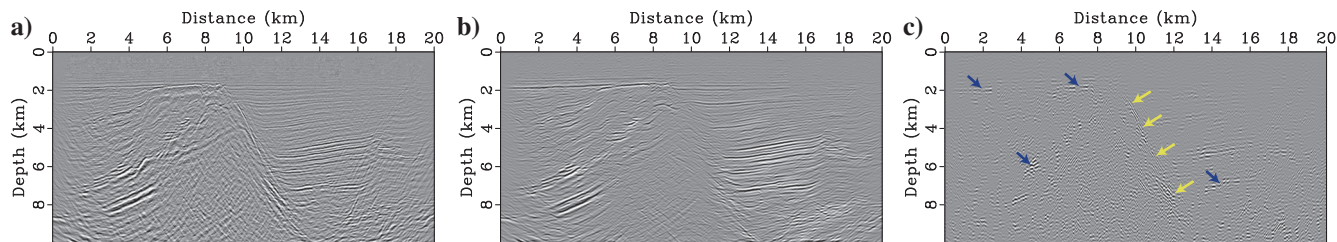


Figure 18. (a) Total, (b) reflector, and (c) diffractor images. (a) Computed using the Gaussian beam depth migration. (b) Calculated by stacking the CNN predicted DACIGs. (c) Computed by adaptively subtracting the (b) stacked reflector image from (a) total image.

of diffraction DACIGs at neighboring locations. Therefore, one issue of the first adaptive subtraction strategy is that there might be residual reflection energy in the diffractor image. This is because, when summing the diffraction DACIGs computed using the adaptive subtraction, even if only one residual diffraction DACIG is inaccurate, the final stacked image for the scatterers might have large artifacts. The two synthetic experiments demonstrate that applying the adaptive subtraction on the stacked image can produce a better result than directly applying adaptive subtracting for the DACIGs.

CONCLUSION

We have developed a new seismic diffraction separation method in the dip-angle domain using an end-to-end CNN. This approach tries to identify and distinguish different geometric characteristics between the reflections and diffractions in the DACIGs, which is then used as a criterion to separate reflections and diffractions. First, we use the trained end-to-end CNN to extract relatively strong reflections in the DACIGs from total DACIGs. Then, two adaptive subtraction strategies are used to compute diffraction DACIGs and stacked images. One is to directly compute the diffraction CIGs by adaptively subtracting the predicted reflection DACIGs from the total gathers, followed by the stacking to yield a diffractor image. The other one is to first calculate a stacked reflector image by summing the predicted reflection DACIGs and then to compute the diffractor image by adaptively subtracting the reflector image from the total stacked image. The experiments for synthetic and field data verify the feasibility and adaptability of the proposed method.

ACKNOWLEDGMENTS

This research is supported by the startup funding (no. 20CX06069A) of Guanghua Scholar in Geophysics Department, at China University of Petroleum (East China). The work is carried out at National Supercomputer Center in Tianjin, and this research is supported by TianHe Qingsuo Project–Special Fund Project in the field of geoscience. We thank the support from the National Outstanding Youth Science Foundation (no. 41922028), the National Natural Science Foundation of China (General Program) (no. 41874149), the Strategic Priority Research Program of the Chinese Academy of Sciences (no. XDA14010303), the Key Program for International Cooperation Projects of China (no. 41720104006), the National Key R&D Program of China (no. 2019YFC0605503), China University of Petroleum (East China) Graduate Innovation Project (no. YCX2021028), the Major Scientific and Technological Projects of CNPC (no. ZD2019183003), the Key Project for Full Node Seismic Processing (no. 30200020-21-ZC0607-0021), and the Funds for Creative Research Groups of China (no. 41821002).

DATA AND MATERIALS AVAILABILITY

Data associated with this research are available and can be obtained by contacting the corresponding author.

REFERENCES

- Aki, K., 1969, Analysis of the seismic coda of local earthquakes as scattered waves: *Journal of Geophysical Research*, **74**, 615–631, doi: [10.1029/JB074i002p00615](https://doi.org/10.1029/JB074i002p00615).
- Audebert, F., P. Froidevaux, H. Rakotoarisoa, and J. Svay-Lucas, 2002, Insights into migration in the angle domain: 72nd Annual International Meeting, SEG, Expanded Abstracts, 1188–1191, doi: [10.1190/1.1816863](https://doi.org/10.1190/1.1816863).
- Bakhtiari Rad, P., B. Schwarz, D. Gajewski, and C. Vanelle, 2018, Common-reflection-surface-based prestack diffraction separation and imaging: *Geophysics*, **83**, no. 1, S47–S55, doi: [10.1190/geo2016-0445.1](https://doi.org/10.1190/geo2016-0445.1).
- Bauer, A., B. Schwarz, and D. Gajewski, 2016, Enhancement of prestack diffraction data and attributes using a traveltime decomposition approach: *Studia Geophysica et Geodaetica*, **60**, 471–486, doi: [10.1007/s11200-015-1278-y](https://doi.org/10.1007/s11200-015-1278-y).
- Bauer, A., J. Walda, and D. Gajewski, 2021, Wavefield decomposition for diffraction separation with convolutional neural networks: First International Meeting for Applied Geoscience & Energy, SEG/AAPG/SEPM.
- Biswas, R., M. K. Sen, V. Das, and T. Mukerji, 2019, Prestack and poststack inversion using a physics-guided convolutional neural network: *Interpretation*, **7**, no. 3, SE161–SE174, doi: [10.1190/INT-2018-0236.1](https://doi.org/10.1190/INT-2018-0236.1).
- Dafni, R., and W. W. Symes, 2017, Diffraction imaging by prestack reverse-time migration in the dip-angle domain: *Geophysical Prospecting*, **65**, 295–316, doi: [10.1111/1365-2478.12580](https://doi.org/10.1111/1365-2478.12580).
- Das, V., A. Pollack, U. Wollner, and T. Mukerji, 2019, Convolutional neural network for seismic impedance inversion: *Geophysics*, **84**, no. 6, R869–R880, doi: [10.1190/geo2018-0838.1](https://doi.org/10.1190/geo2018-0838.1).
- Dell, S., and D. Gajewski, 2011, Common-reflection-surface-based workflow for diffraction imaging: *Geophysics*, **76**, no. 5, S187–S195, doi: [10.1190/geo2010-0229.1](https://doi.org/10.1190/geo2010-0229.1).
- Di, H., Z. Wang, and G. AlRegib, 2018, Deep convolutional neural networks for seismic salt-body delineation: Presented at the Annual Convention and Exhibition, AAPG.
- Fomel, S., E. Landa, and M. T. Taner, 2007, Poststack velocity analysis by separation and imaging of seismic diffractions: *Geophysics*, **72**, no. 6, U89–U94, doi: [10.1190/1.2781533](https://doi.org/10.1190/1.2781533).
- Harlan, W. S., J. F. Claerbout, and F. Rocca, 1984, Signal/noise separation and velocity estimation: *Geophysics*, **49**, 1869–1880, doi: [10.1190/1.1441600](https://doi.org/10.1190/1.1441600).
- He, K., X. Zhang, S. Ren, and J. Sun, 2015, Delving deep into rectifiers: Surpassing human-level performance on ImageNet classification: Proceedings of the IEEE International Conference on Computer Vision, 1026–1034.
- Herrmann, F. J., D. Wang, and D. J. Verschuur, 2008, Adaptive curvelet-domain primary-multiple separation: *Geophysics*, **73**, no. 3, A17–A21, doi: [10.1190/1.2904986](https://doi.org/10.1190/1.2904986).
- Hill, N. R., 1990, Gaussian beam migration: *Geophysics*, **55**, 1416–1428, doi: [10.1190/1.1442788](https://doi.org/10.1190/1.1442788).
- Hollander, Y., A. Merouane, and O. Yilmaz, 2018, Using a deep convolutional neural network to enhance the accuracy of first-break picking: 88th Annual International Meeting, SEG, Expanded Abstracts, 4628–4632, doi: [10.1190/segam2018-2982650.1](https://doi.org/10.1190/segam2018-2982650.1).
- Ioffe, S., and C. Szegedy, 2015, Batch normalization: Accelerating deep network training by reducing internal covariate shift: International Conference on Machine Learning, 448–456.
- Jin, Y., W. Hu, X. Wu, and J. Chen, 2018, Learn low wavenumber information in FWI via deep inception based convolutional networks: 88th An-

- nual International Meeting, SEG, Expanded Abstracts, 2091–2095, doi: [10.1190/segam2018-2997901.1](https://doi.org/10.1190/segam2018-2997901.1).
- Kanasewich, E. R., and S. M. Phadke, 1988, Imaging discontinuities on seismic sections: *Geophysics*, **53**, 334–345, doi: [10.1190/1.1442467](https://doi.org/10.1190/1.1442467).
- Karchevskiy, M., I. Ashrapov, and L. Kozinkin, 2018, Automatic salt deposits segmentation: A deep learning approach: arXiv preprint, arXiv: 1812.01429.
- Khaidukov, V., E. Landa, and T. J. Moser, 2004, Diffraction imaging by focusing-defocusing: An outlook on seismic superresolution: *Geophysics*, **69**, 1478–1490, doi: [10.1190/1.1836821](https://doi.org/10.1190/1.1836821).
- Kingma, D. P., and J. Ba, 2014, Adam: A method for stochastic optimization: arXiv preprint, arXiv:1412.6980.
- Klokov, A., R. Bain, and E. Landa, 2010a, Separation and imaging of seismic diffractions in dip angle domain: 72nd Annual International Conference and Exhibition, EAGE, Extended Abstracts, doi: [10.3997/2214-4609.201400838](https://doi.org/10.3997/2214-4609.201400838).
- Klokov, A., R. Bain, E. Landa, P. Thore, and I. Tarrass, 2010b, Diffraction imaging for fracture detection: Synthetic case study: 80th Annual International Meeting, SEG, Expanded Abstracts, 3354–3358, doi: [10.1190/1.3513545](https://doi.org/10.1190/1.3513545).
- Klokov, A., and S. Fomel, 2012, Separation and imaging of seismic diffractions using migrated dip-angle gathers: *Geophysics*, **77**, no. 6, S131–S143, doi: [10.1190/geo2012-0017.1](https://doi.org/10.1190/geo2012-0017.1).
- Krey, T., 1952, The significance of diffraction in the investigation of faults: *Geophysics*, **17**, 843–858, doi: [10.1190/1.1437815](https://doi.org/10.1190/1.1437815).
- Kunz, B. F., 1960, Diffraction problems in fault interpretation: *Geophysical Prospecting*, **8**, 381–388, doi: [10.1111/j.1365-2478.1960.tb01722.x](https://doi.org/10.1111/j.1365-2478.1960.tb01722.x).
- Landa, E., S. Fomel, and M. Reshef, 2008, Separation, imaging, and velocity analysis of seismic diffractions using migrated dip-angle gathers: 78th Annual International Meeting, SEG, Expanded Abstracts, 2176–2180, doi: [10.1190/1.3059318](https://doi.org/10.1190/1.3059318).
- Landa, E., V. Shtivelman, and B. Gelchinsky, 1987, A method for detection of diffracted waves on common-offset sections: *Geophysical Prospecting*, **35**, 359–373, doi: [10.1111/j.1365-2478.1987.tb00823.x](https://doi.org/10.1111/j.1365-2478.1987.tb00823.x).
- Li, C., J. Zhao, S. Peng, X. Cui, and P. Lin, 2020, Separating and imaging diffractions of seismic waves in the full-azimuth dip-angle domain: *Journal of Geophysics and Engineering*, **17**, 339–356, doi: [10.1093/jge/gxz110](https://doi.org/10.1093/jge/gxz110).
- Mantovani, R. G., A. L. Rossi, J. Vanschoren, B. Bischi, and A. C. Carvalho, 2015, To tune or not to tune: Recommending when to adjust SVM hyperparameters via meta-learning: International Joint Conference on Neural Networks, 1–8.
- Papziner, U., and K.-P. Nick, 1998, Automatic detection of hyperbolas in georadarograms by slant-stack processing and migration: *First Break*, **16**, 219–223, doi: [10.1046/j.1365-2397.1998.00691.x](https://doi.org/10.1046/j.1365-2397.1998.00691.x).
- Pochet, A., P. H. Diniz, H. Lopes, and M. Gattass, 2018, Seismic fault detection using convolutional neural networks trained on synthetic post-stacked amplitude maps: *IEEE Geoscience and Remote Sensing Letters*, **16**, 352–356, doi: [10.1109/LGRS.2018.2875836](https://doi.org/10.1109/LGRS.2018.2875836).
- Reshef, M., and E. Landa, 2009, Post-stack velocity analysis in the dip-angle domain using diffractions: *Geophysical Prospecting*, **57**, 811–821, doi: [10.1111/j.1365-2478.2008.00773.x](https://doi.org/10.1111/j.1365-2478.2008.00773.x).
- Riley, D. C., and J. F. Claerbout, 1976, 2-D multiple reflections: *Geophysics*, **41**, 592–620, doi: [10.1190/1.1440638](https://doi.org/10.1190/1.1440638).
- Ronen, J., and J. F. Claerbout, 1985, Surface-consistent residual statics estimation by stack-power maximization: *Geophysics*, **50**, 2759–2767, doi: [10.1190/1.1441896](https://doi.org/10.1190/1.1441896).
- Sato, H., 1977, Energy propagation including scattering effects single isotropic scattering approximation: *Journal of Physics of the Earth*, **25**, 27–41, doi: [10.4294/jpe1952.25.27](https://doi.org/10.4294/jpe1952.25.27).
- Schwarz, B., 2019, Coherent wavefield subtraction for diffraction separation: *Geophysics*, **84**, no. 3, V157–V168, doi: [10.1190/geo2018-0368.1](https://doi.org/10.1190/geo2018-0368.1).
- Shi, Y., X. Wu, and S. Fomel, 2018, Automatic salt-body classification using a deep convolutional neural network: 88th Annual International Meeting, SEG, Expanded Abstracts, 1971–1975, doi: [10.1190/segam2018-2997304.1](https://doi.org/10.1190/segam2018-2997304.1).
- Taner, M. T., S. Fomel, and E. Landa, 2006, Separation and imaging of seismic diffractions using plane-wave decomposition: 76th Annual International Meeting, SEG, Expanded Abstracts, 2401–2405, doi: [10.1190/1.2370017](https://doi.org/10.1190/1.2370017).
- Tschannen, V., N. Ettrich, M. Delescluse, and J. Keuper, 2020, Detection of point scatterers using diffraction imaging and deep learning: *Geophysical Prospecting*, **68**, 830–844, doi: [10.1111/1365-2478.12889](https://doi.org/10.1111/1365-2478.12889).
- Waldegaard, A., and A. Solberg, 2017, Salt classification using deep learning: 79th Annual International Conference and Exhibition, EAGE, Extended Abstracts, doi: [10.3997/2214-4609.201700918](https://doi.org/10.3997/2214-4609.201700918).
- Wang, F., and S. Chen, 2019, Residual learning of deep convolutional neural network for seismic random noise attenuation: *IEEE Geoscience and Remote Sensing Letters*, **16**, 1314–1318, doi: [10.1109/LGRS.2019.2895702](https://doi.org/10.1109/LGRS.2019.2895702).
- Wang, K., L. Bandura, D. Bevc, S. Cheng, J. DiSiena, A. Halpert, K. Ossipov, B. Power, and E. Xu, 2019, End-to-end deep neural network for seismic inversion: 89th Annual International Meeting, SEG, Expanded Abstracts, 4982–4985, doi: [10.1190/segam2019-3216464.1](https://doi.org/10.1190/segam2019-3216464.1).
- Wang, Y.-Q., Q. Wang, W.-K. Lu, Q. Ge, and X.-F. Yan, 2022, Seismic impedance inversion based on cycle-consistent generative adversarial network: *Petroleum Science*, **19**, 147–161, doi: [10.1016/j.petsci.2021.09.038](https://doi.org/10.1016/j.petsci.2021.09.038).
- Wu, X., Z. Geng, Y. Shi, N. Pham, S. Fomel, and G. Caumon, 2020, Building realistic structure models to train convolutional neural networks for seismic structural interpretation: *Geophysics*, **85**, no. 4, WA27–WA39, doi: [10.1190/geo2019-0375.1](https://doi.org/10.1190/geo2019-0375.1).
- Wu, X., L. Liang, Y. Shi, and S. Fomel, 2019a, FaultSeg3D: Using synthetic data sets to train an end-to-end convolutional neural network for 3D seismic fault segmentation: *Geophysics*, **84**, no. 3, IM35–IM45, doi: [10.1190/geo2018-0646.1](https://doi.org/10.1190/geo2018-0646.1).
- Wu, X., Y. Shi, S. Fomel, and L. Liang, 2018, Convolutional neural networks for fault interpretation in seismic images: 88th Annual International Meeting, SEG, Expanded Abstracts, 1946–1950, doi: [10.1190/segam2018-2995341.1](https://doi.org/10.1190/segam2018-2995341.1).
- Wu, X., Y. Shi, S. Fomel, L. Liang, Q. Zhang, and A. Z. Yusifov, 2019b, FaultNet3D: Predicting fault probabilities, strikes, and dips with a single convolutional neural network: *IEEE Transactions on Geoscience and Remote Sensing*, **57**, 9138–9155, doi: [10.1109/TGRS.2019.2925003](https://doi.org/10.1109/TGRS.2019.2925003).
- Wu, Y., and Y. Lin, 2019, InversionNet: An efficient and accurate data-driven full waveform inversion: *IEEE Transactions on Computational Imaging*, **6**, 419–433, doi: [10.1109/TCI.2019.2956866](https://doi.org/10.1109/TCI.2019.2956866).
- Wu, Y., and G. A. McMechan, 2018, Feature-capturing full waveform inversion using a convolutional neural network: 88th Annual International Meeting, SEG, Expanded Abstracts, 2061–2065, doi: [10.1190/segam2018-2963265.1](https://doi.org/10.1190/segam2018-2963265.1).
- Xiong, W., X. Ji, Y. Ma, Y. Wang, N. M. AlBinHassan, M. N. Ali, and Y. Luo, 2018, Seismic fault detection with convolutional neural network: *Geophysics*, **83**, no. 5, O97–O103, doi: [10.1190/geo2017-0666.1](https://doi.org/10.1190/geo2017-0666.1).
- Yang, J., J. Huang, Z. Li, H. Zhu, G. McMechan, J. Zhang, C. Hu, and Y. Zhao, 2021, Mitigating velocity errors in least-squares imaging using angle-dependent forward and adjoint Gaussian beam operators: *Surveys in Geophysics*, **42**, 1305–1346, doi: [10.1007/s10712-021-09676-y](https://doi.org/10.1007/s10712-021-09676-y).
- Yilmaz, O. G., and J. F. Claerbout, 1980, Prestack partial migration: *Geophysics*, **45**, 1753–1779, doi: [10.1190/1.1441064](https://doi.org/10.1190/1.1441064).
- Yu, S., J. Ma, and W. Wang, 2019, Deep learning for denoising: *Geophysics*, **84**, no. 6, V333–V350, doi: [10.1190/geo2018-0668.1](https://doi.org/10.1190/geo2018-0668.1).
- Yuan, S., J. Liu, S. Wang, T. Wang, and P. Shi, 2018, Seismic waveform classification and first-break picking using convolution neural networks: *IEEE Geoscience and Remote Sensing Letters*, **15**, 272–276, doi: [10.1109/LGRS.2017.2785834](https://doi.org/10.1109/LGRS.2017.2785834).
- Zhang, J., and J. Zhang, 2014, Diffraction imaging using shot and opening-angle gathers: A prestack time migration approach: *Geophysics*, **79**, no. 2, S23–S33, doi: [10.1190/geo2013-0016.1](https://doi.org/10.1190/geo2013-0016.1).
- Zhang, K., W. Zuo, Y. Chen, D. Meng, and L. Zhang, 2017, Beyond a Gaussian denoiser: Residual learning of deep CNN for image denoising: *IEEE Transactions on Image Processing*, **26**, 3142–3155, doi: [10.1109/TIP.2017.2662206](https://doi.org/10.1109/TIP.2017.2662206).
- Zhao, J., S. Peng, W. Du, and X. Li, 2016, Diffraction imaging method by Mahalanobis-based amplitude damping: *Geophysics*, **81**, no. 6, S399–S408, doi: [10.1190/geo2015-0692.1](https://doi.org/10.1190/geo2015-0692.1).
- Zheng, Y., Q. Zhang, A. Yusifov, and Y. Shi, 2019, Applications of supervised deep learning for seismic interpretation and inversion: *The Leading Edge*, **38**, 526–533, doi: [10.1190/tle38070526.1](https://doi.org/10.1190/tle38070526.1).

Biographies and photographs of the authors are not available.